Theoretical and Photoluminescence Studies on the $d^{10}-s^2$ Au^I-Tl^I Interaction in Extended Unsupported Chains

Eduardo J. Fernández,[b] **Antonio Laguna,***[a] **José M. López-de-Luzuriaga,**[b]
Fernando Mendizabal,[c] **Miguel Monge,**[b] **M. Elena Olmos,**[b] **and Javier Pérez**[b]

Abstract: The reactions of solutions of $TlPF_6$ and $OPPh_3$ in tetrahydrofuran or acetone with $NBu_4[AuR_2]$ ($R = C_6Cl_5$, C_6F_5) gave the new complexes $[Au(C_6Cl_5)_2]_2[Tl(OPPh_3)][Tl(OPPh_3)(L)]$ (L = THF (**1**), acetone (**2**)) and the previously reported $[Tl(OPPh_3)_2][Au(C_6F_5)_2]$ (**3**). The crystal structures of complexes **1** and **2** display extended unsupported chains with short intermolecular interactions between alternating gold(I) and thallium(I) centres. Moreover, the Tl^I centres show two different types of geometrical environments, such as pseudotetrahedral and distorted trigonal-bipyramidal, due to the presence of solvent molecules that act as ligands in the solid-state structure. Quasirelativistic and nonrelativistic ab initio calculations were performed to study the nature of the intermetallic Au^I-Tl^I interactions and are consistent with the presence of a high ionic contribution (80%) and dispersion-type (van der Waals) interaction with a charge-transfer contribution (20%) when relativistic effects are taken into account. All complexes are luminescent in the solid state at room temperature and at 77 K. Complexes **1** and **2** show site-selective excitation, probably due to the different environments around the Tl^I centres. The DFT and time-dependent (TD)-DFT calculations are in agreement with the experimental excitation spectra for all complexes and confirm the site-selective excitation behaviour as a function of the Tl^I geometrical environment.

Keywords: ab initio calculations · density functional calculations · gold · luminescence · thallium

Introduction

In the last few years bonding interactions between closed-shell metal atoms have been widely studied from theoretical and experimental points of view.[1] Among the heavy metals, gold–gold interactions (aurophilicity) have received close attention, since d^{10} Au^I ions have a great ability to form dimers, oligomers, and polymers based on these interactions, which are comparable in strength to hydrogen bonds.[2] In addition, some of these complexes display very interesting photophysical properties such as luminescence, also induced, among other factors, by the presence of intermetallic interactions.[3]

More recent studies deal with gold(I)-containing heterometallic compounds in which short closed-shell metal–metal interactions are present (metallophilicity).[1] Thus, for example, Au^I-Pd^{II} ($d^{10}-d^8$),[4] Au^I-Ag^I ($d^{10}-d^{10}$)[5] and Au^I-Cu^I ($d^{10}-d^{10}$)[5] interactions have been theoretically described by using correlated methods, and it was shown that the metallophilic interactions arise from dispersion-type (van der Waals), correlation effects and charge-transfer contributions.[4, 6] Moreover, the generation of Au–M interactions by acid-base reactions of, for instance, Tl^+ or Ag^+ Lewis acid precursors with $[AuR_2]^-$ ($R = C_6F_5$ or C_6Cl_5) Lewis bases, provides an additional electrostatic attraction.[7–9]

Some of these Au^I–metal complexes have proved to be a new class of photoluminescent materials in which the emission of radiation results mainly from the interactions between the different metal centres.[10] Among this class of materials we have focused on the study of the $d^{10}-s^2$ interaction between Au^I and Tl^I ions.[8, 9] Previous work by Fackler et al. showed interesting luminescence properties of an extended Au–Tl chain with bridging ligands,[11] as well as the sandwich-type complex $[Tl\{Au(\mu\text{-}C^2\text{-}N^3\text{-Rim})\}_3]^+$ (C^2-N^3-Rim = 1-benzylimidazolate, 1-methylimidazolate),[12] in which the emissive properties arise from the intermetallic interactions. Catalano et al. reported novel gold metallocryptates in

---

[a] Prof. A. Laguna
Departamento de Química Inorgánica
Instituto de Ciencia de Materiales de Aragón
Universidad de Zaragoza-CSIC
50009 Zaragoza (Spain)
E-mail: alaguna@posta.unizar.es.

[b] Dr. E. J. Fernández, Dr. J. M. López-de-Luzuriaga,
Dr. M. Monge, Dr. M. E. Olmos, J. Pérez
Departamento de Química, Universidad de la Rioja
Grupo de Síntesis Química de La Rioja, UA-CSIC
Complejo Científico Tecnológico
26001 Logroño (Spain)

[c] Dr. F. Mendizabal
Departamento de Química, Facultad de Ciencias
Universidad de Chile, Casilla 653-Santiago (Chile)

0947-6539/03/0902-0456 $ 20.00+.50/0

which trigonal Au^I host complexes encapsulate Tl^I ions and display a rich photoluminescence behaviour.[13] We recently developed another strategy for the synthesis of Au–Tl complexes by treating $[AuR_2]^-$ Lewis base precursors with Tl^I salts that act as Lewis acids. Thus, we reported the synthesis and luminescence behaviour of the first unsupported gold–thallium chain $[Tl(OPPh_3)_2][Au(C_6F_5)_2]$ (**3**)[8] and new two- and three-dimensional arrays of the type $[Tl(4,4'\text{-bipy})_n][AuR_2]$ (bipy = bipyridine; R = C_6F_5, C_6Cl_5),[9] in which variation of the perhalophenyl ligands gives rise to different structural arrangements. Recently, Gade gave an overview of d^{10}–s^2 interactions between Au^I, Pd^0 and Pt^0 d^{10} ions and Tl^I s^2 ion.[14]

Here we report the synthesis of and luminescence studies on the new complexes $[Au(C_6Cl_5)_2]_2[Tl(OPPh_3)][Tl(OPPh_3)(L)]$ (L = THF (**1**), acetone (**2**)) and compare them with the previously reported $[Tl(OPPh_3)_2][Au(C_6F_5)_2]$ (**3**). We also carried out ab initio calculations at HF and MP2 levels of theory on simplified model systems with nonrelativistic and relativistic effective core potentials to study the nature of the d^{10}–s^2 Au^I–Tl^I interaction. Finally, we performed time-dependent DFT (TD-DFT) calculations, which allow the excitations that lead to the emission of radiation in the solid state to be predicted.

Results and Discussion

Synthesis and structure: Complexes $[Au(C_6Cl_5)_2]_2[Tl(OPPh_3)][Tl(OPPh_3)(L)]$ (L = THF (**1**), acetone (**2**)) were obtained by addition of $TlPF_6$ (1 equiv) and $OPPh_3$ (1 or 2 equiv) to a solution of $NBu_4[Au(C_6Cl_5)_2]$ (1 equiv) in tetrahydrofuran (**1**) or acetone (**2**). The already described unsupported chain $[Tl(OPPh_3)_2][Au(C_6F_5)_2]$ (**3**) was synthesised from precursors other than those previously reported,[8] in the same way as **1** and **2**. Thus, addition of $TlPF_6$ and $OPPh_3$ to a solution of $NBu_4[Au(C_6F_5)_2]$ in a 1:2:1 molar ratio in tetrahydrofuran led to the synthesis of **3** in a good yield. Complexes **1** and **2** were collected as crystals by slow diffusion of *n*-hexane into THF and acetone solutions respectively, whereas complex **3** was isolated as a yellow-green solid. All complexes are soluble in acetone and tetrahydrofuran and insoluble in diethyl ether and *n*-hexane, and their elemental analyses and physical and spectroscopic properties are in agreement with the proposed formulas. As we previously reported,[8, 9] such Au–Tl compounds, derived from acid–base reactions of the metalloligand $[AuR_2]^-$, dissociate in solution to give the separate ionic counterparts (1:1 electrolyte behaviour). This was also confirmed by the ^{19}F NMR spectrum of **3**, which resembles the pattern of the precursor $NBu_4[Au(C_6F_5)_2]$. The $^{31}P\{^1H\}$ NMR spectra show one singlet for the $OPPh_3$ ligands at $\delta = 26.5$ (**1**), 26.7 (**2**) and 30.0 ppm (**3**). The ^1H NMR spectra show signals for THF at $\delta = 3.43$ and 1.86 ppm (**1**) or acetone at $\delta = 2.09$ ppm (**2**). The IR spectra show, among others, absorptions of the C_6Cl_5 and C_6F_5 ligands bonded to gold(I) at 614 and 835 cm^{-1} (**1**), 615 and 836 cm^{-1} (**2**) and 784, 957 and 1503 cm^{-1} (**3**) and the P=O stretching band at 1156 (**1**), 1156 (**2**) and 1178 cm^{-1} (**3**). In addition, **2** shows a band at 1702 cm^{-1} for the $\nu(C=O)$ stretch of the acetone molecule coordinated to Tl^I.

Abstract in Spanish: *La reacción de una disolución de* $TlPF_6$ *y* $OPPh_3$ *en tetrahidrofurano o acetona con* $NBu_4[AuR_2]$ *(R =* C_6Cl_5, C_6F_5*) conduce a la síntesis de los nuevos complejos* $[Au(C_6Cl_5)_2]_2[Tl(OPPh_3)][Tl(OPPh_3)(L)]$ *(L = THF (**1**), acetona (**2**)) o el anteriormente descrito* $[Tl(OPPh_3)_2][Au(C_6F_5)_2]$ *(**3**). Las estructuras cristalinas de los complejos **1** y **2** muestran cadenas infinitas en las que se observan interacciones intermoleculares cortas entre centros alternos de oro(I) y talio(I). Además, los centros de* Tl^I *presentan dos tipos de entorno geométrico diferente: pseudotetraédrico y de bipirámide trigonal distorsionado, debido a la presencia de moléculas de disolvente actuando como ligandos en la estructura en estado sólido. Se han llevado a cabo cálculos ab initio quasirelativistas y no-relativistas con objeto de estudiar la naturaleza de las interacciones intermetálicas* Au^I-Tl^I*, siendo consistentes con la presencia de una elevada contribución iónica (80 %) y de dispersión (van der Waals) con contribuciones de transferencia de carga (20 %) cuando se tienen en cuenta los efectos relativistas. Todos los compuestos son luminiscentes en estado sólido, tanto a temperatura ambiente como a 77 K. Los complejos **1** y **2** muestran una excitación selectiva probablemente debida a los diferentes entornos de los centros de* Tl^I*. Los cálculos DFT y TD-DFT están de acuerdo con los espectros de excitación experimentales para todos los compuestos y confirman que la excitación selectiva depende de la disposición geométrica de los centros de* Tl^I*.*

The crystal structures of complexes **1** and **2** were established by X-ray diffraction studies (Figure 1, Figure 2, Figure 3 and Figure 4; Table 1, Table 2 and Table 3), and in both cases the asymmetric unit contains four metal atoms (instead of two as observed in **3**)[8] with a Tl-Au-Tl-Au arrangement. They display short metal–metal interactions with Au···Tl distances in the range 3.0529(3)–3.3205(3) Å for **1** and 3.0937(3)–3.2705(4) Å for **2**. Both compounds form one-dimensional polymers in which the gold(I) centres are linearly coordinated

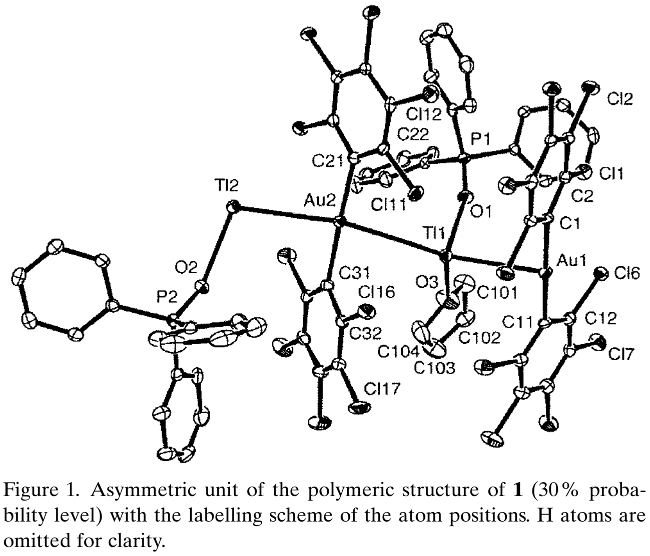

Figure 1. Asymmetric unit of the polymeric structure of **1** (30 % probability level) with the labelling scheme of the atom positions. H atoms are omitted for clarity.

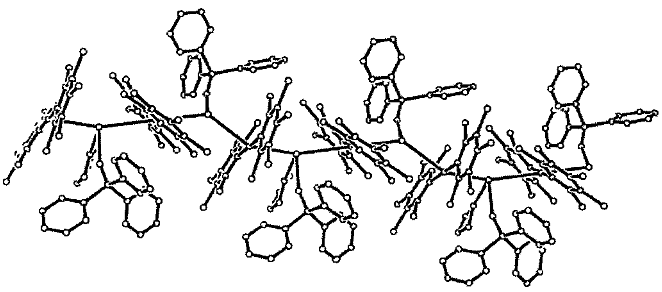

Figure 2. Molecular structure of **1**. H atoms are omitted for clarity.

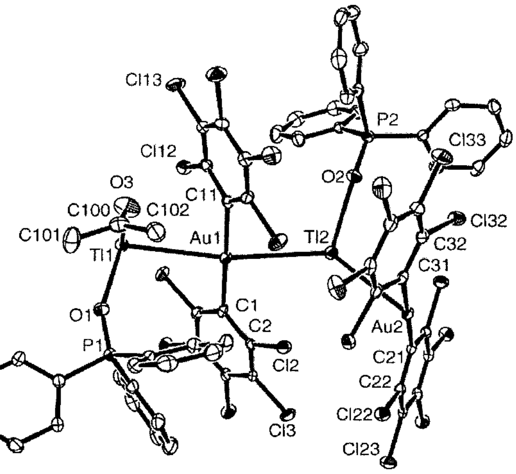

Figure 3. Asymmetric unit of polymeric structure of complex **2** (30% probability level) with the labelling scheme of the atom positions. H atoms are omitted for clarity.

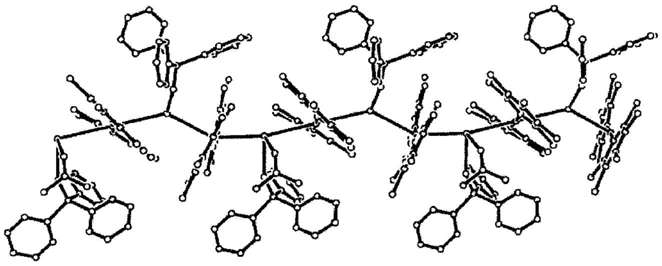

Figure 4. Molecular structure of complex **2**. H atoms are omitted for clarity.

to two C_6Cl_5 groups with Au–C distances in the range 2.041(5)–2.058(4) Å for **1** and 2.038(7)–2.055(6) Å for **2**. In contrast, each thallium atom of the asymmetric unit (Figure 1 and Figure 3) has a different environment: while Tl1 is ligated by the oxygen atoms of a $OPPh_3$ ligand and a solvent molecule (THF (**1**) or acetone (**2**)) and has a trigonal-bipyramidal geometry with a vacant equatorial coordination site (presumably associated with the stereochemically active lone pair), Tl2 only bears a $OPPh_3$ ligand and has a strongly distorted tetrahedral geometry with a vacant coordination site. In both **1** and **2**, the Tl–O bond lengths for the $OPPh_3$ ligands are shorter than those of THF or acetone ligands. Thus, while the Tl–$OPPh_3$ distances are 2.471(3) and 2.582(4) in **1** and 2.511(4) and 2.572(4) Å in **2** (similar to those in **3**: 2.483(3) and 2.550(4) Å), the solvent molecules are only weakly coordinated, with Tl–O distances clearly longer than the

Table 1. Details of data collection and structure refinement for complexes **1** and **2**.

Compound	1	2
empirical formula	$C_{64}H_{38}Au_2Cl_{20}O_3P_2Tl_2$	$C_{63}H_{36}Au_2Cl_{20}O_3P_2Tl_2$
crystal habit	yellow plate	yellow plate
crystal size [mm]	0.45 × 0.20 × 0.10	0.50 × 0.28 × 0.11
crystal system	triclinic	monoclinic
space group	$P\bar{1}$	$P2_1/c$
a [Å]	11.8699(1)	12.0687(1)
b [Å]	14.2869(2)	13.9416(1)
c [Å]	21.8171(3)	42.5190(5)
α [°]	80.8126(5)	90
β [°]	82.6669(6)	94.349(4)
γ [°]	87.7221(8)	90
V [Å^3]	3621.79(8)	7133.52(11)
Z	2	4
ρ_{calcd} [g cm^{-3}]	2.227	2.248
M	2428.56	2414.53
F(000)	2272	4512
T [°C]	−100	−100
$2\theta_{max}$ [°]	56	56
μMo$_{K\alpha}$) [mm^{-1}]	9.301	9.444
transmission	0.4565, 0.1025	0.4231, 0.0882
no. of reflns measured	52126	17857
no. of unique reflns	17071	10701
R_{int}	0.047	0.0218
R ($F > 2\sigma(F)$)[a]	0.0331	0.0354
wR (F^2, all reflns)[b]	0.0717	0.0576
no. of reflns used	17071	10701
no. of parameters	838	831
no. of restraints	258	255
S[c]	1.034	1.102
max. residual electron density [e Å^{-3}]	1.273	0.729

[a] $R(F)=\Sigma||F_o|-|F_c||/\Sigma|F_o|$. [b] $wR(F^2)=[\Sigma\{w(F_o^2-F_c^2)^2\}/\Sigma\{w(F_o^2)^2\}]^{0.5}$; $w^{-1}=\sigma^2(F_o^2)+(aP)^2+bP$, where $P=[F_o^2+2F_c^2]/3$ and a and b are constants adjusted by the program. [c] $S=[\Sigma\{w(F_o^2-F_c^2)^2\}/(n-p)]^{0.5}$, where n is the number of data and p the number of parameters.

Table 2. Selected bond lengths [Å] and angles [°] for **1**.[a]

Au(1)–C(11)	2.055(5)	Au(1)–C(1)	2.058(4)
Au(2)–C(21)	2.041(5)	Au(2)–C(31)	2.051(5)
Au(1)–Tl(1)	3.0529(3)	Au(1)–Tl(2)#1	3.1630(3)
Au(2)–Tl(2)	3.1452(3)	Au(2)–Tl(1)	3.3205(3)
Tl(1)–O(1)	2.471(3)	Tl(1)–O(3)	2.766(5)
Tl(2)–O(2)	2.582(4)	O(1)–P(1)	1.495(4)
O(2)–P(2)	1.498(4)	O(3)–C(104)	1.401(9)
O(3)–C(101)	1.412(8)	C(101)–C(102)	1.487(9)
C(102)–C(103)	1.499(10)	C(103)–C(104)	1.473(11)
C(11)-Au(1)-C(1)	178.10(18)	C(11)-Au(1)-Tl(1)	89.21(12)
C(1)-Au(1)-Tl(1)	91.47(12)	C(11)-Au(1)-Tl(2)#1	80.09(12)
C(1)-Au(1)-Tl(2)#1	100.40(12)	Tl(1)-Au(1)-Tl(2)#1	142.608(8)
C(21)-Au(2)-C(31)	176.69(17)	C(21)-Au(2)-Tl(2)	94.54(13)
C(31)-Au(2)-Tl(2)	87.34(13)	C(21)-Au(2)-Tl(1)	96.74(13)
C(31)-Au(2)-Tl(1)	81.50(13)	Tl(2)-Au(2)-Tl(1)	168.529(8)
O(1)-Tl(1)-O(3)	79.65(14)	O(1)-Tl(1)-Au(1)	92.33(9)
O(3)-Tl(1)-Au(1)	96.31(12)	O(1)-Tl(1)-Au(2)	94.80(9)
O(3)-Tl(1)-Au(2)	106.92(12)	Au(1)-Tl(1)-Au(2)	156.560(9)
O(2)-Tl(2)-Au(2)	102.56(8)	O(2)-Tl(2)-Au(1)#2	115.37(9)
Au(2)-Tl(2)-Au(1)#2	131.599(8)	P(1)-O(1)-Tl(1)	162.6(2)
P(2)-O(2)-Tl(2)	146.7(2)	C(104)-O(3)-C(101)	107.9(6)
C(104)-O(3)-Tl(1)	123.5(4)	C(101)-O(3)-Tl(1)	125.5(4)
O(3)-C(101)-C(102)	106.3(6)	C(101)-C(102)-C(103)	104.5(6)
C(104)-C(103)-C(102)	105.6(6)	O(3)-C(104)-C(103)	107.9(6)

[a] Symmetry transformations used to generate equivalent atoms: #1: $x-1$, y, z; #2: $x+1$, y, z.

Table 3. Selected bond lengths [Å] and angles [°] for **2**.[a]

Au(1)−C(1)	2.055(6)	Au(1)−C(11)	2.055(6)
Au(2)−C(31)	2.038(7)	Au(2)−C(21)	2.041(7)
Au(1)−Tl(2)	3.2438(3)	Au(1)−Tl(1)	3.2705(4)
Au(2)−Tl(1)#1	3.0937(3)	Au(2)−Tl(2)	3.1492(3)
Tl(1)−O(1)	2.511(4)	Tl(1)−O(3)	2.828(7)
Tl(2)−O(2)	2.572(4)	O(1)−P(1)	1.488(4)
P(2)−O(2)	1.495(4)	O(3)−C(100)	1.211(9)
C(100)−C(102)	1.481(10)	C(100)−C(101)	1.484(11)
C(1)-Au(1)-C(11)	178.2(2)	C(1)-Au(1)-Tl(2)	95.50(15)
C(11)-Au(1)-Tl(2)	85.46(15)	C(1)-Au(1)-Tl(1)	97.53(15)
C(11)-Au(1)-Tl(1)	81.59(15)	Tl(2)-Au(1)-Tl(1)	166.738(12)
C(31)-Au(2)-C(21)	178.6(2)	C(31)-Au(2)-Tl(1)#1	88.75(15)
C(21)-Au(2)-Tl(1)#1	91.98(14)	C(31)-Au(2)-Tl(2)	78.54(15)
C(21)-Au(2)-Tl(2)	101.49(15)	Tl(1)#1-Au(2)-Tl(2)	143.881(10)
O(1)-Tl(1)-O(3)	79.35(17)	O(1)-Tl(1)-Au(2)#2	87.31(10)
O(3)-Tl(1)-Au(2)#2	107.42(13)	O(1)-Tl(1)-Au(1)	100.96(10)
O(3)-Tl(1)-Au(1)	93.88(13)	Au(2)#2-Tl(1)-Au(1)	158.308(14)
O(2)-Tl(2)-Au(2)	107.23(9)	O(2)-Tl(2)-Au(1)	108.88(10)
Au(2)-Tl(2)-Au(1)	135.725(10)	P(1)-O(1)-Tl(1)	151.7(3)
P(2)-O(2)-Tl(2)	145.6(3)	C(100)-O(3)-Tl(1)	128.0(6)
O(3)-C(100)-C(102)	121.9(8)	O(3)-C(100)-C(101)	122.2(8)
C(102)-C(100)-C(101)	115.9(8)		

[a] Symmetry transformations used to generate equivalent atoms: #1: $x+1$,y, z; #2: $x-1$, y, z.

sum of the covalent radii (2.21 Å), but within the sum of van der Waals radii of thallium and oxygen (ca. 3.35 Å). The Tl−O(THF) distance in **1** is 2.766(5) Å, similar to those observed in $[(thf)_2Tl(\mu\text{-}NC)Mn(CO)(dppm)_2]PF_6$ (dppm = bis(dimethylphosphanyl)methane); 2.74(3) and 2.75(3) Å),[15] $[Tl(tpp)(OSO_2CF_3)(thf)\cdot(THF)]$ (tpp = tetraphenylporphyrinato; 2.778(7) Å)[16] and $[Tl(bipy)][Tl(bipy)_{0.5}(thf)][Au(C_6Cl_5)_2]_2$ (2.781(7) Å),[9] but shorter than the that in $\{[Tl(Me)_2(thf)(O_2C_6H(Me)(t\mathrm{Bu}))]_2\}_n$ (2.862(3) Å),[17] and the Tl−O (acetone) distance in **2** is 2.828(7) Å, like that observed in the polymeric $\{trans,trans,trans\text{-}[PtTl_2(C_6F_5)_2(C{\equiv}C t\mathrm{Bu})_2](acetone)_2\}_n$ (2.83(2) Å)[18] and comparable to those found in other complexes.[19–21] Finally, a series of Au ··· Cl and Tl ··· Cl contacts between atoms of the same linear chain (in the range 3.2874(12) – 3.6380(15) (**1**) or 3.289(2)-3.4449(16) Å (**2**)) and some Tl ··· Cl interactions between adjacent chains (in the range 3.5319(14) – 3.7459(14) (**1**) or 3.4450(21) – 3.6472(20) Å (**2**)) may contribute to the stability of the compounds.

Ab initio calculations: metallophilic attraction: The geometries of the $[Tl(OPH_3)_2]^+$ and $[Au(C_6H_5)_2]^-$ fragments were fully optimised at the MP2 level of theory. A C_{2v} point symmetry was assumed for the thallium fragment, while a D_{2h} symmetry was used for the gold anion. The optimised distances and angles are given in Table 4 and Table 5 with experimental data from X-ray diffraction studies for comparison.[8]

Table 4. Optimised distances [pm] and angles [°] for $[Tl(OPH_3)_2]^+$ at the MP2 level.

Parameter	Tl[3-VE] QR	Tl[3-VE] NR	Experimental
P−H	141.5	141.0	–
P−O	154.9	155.9	149
Tl−O	246.7	224.3	248 – 255
P-O-Tl	165.5	143.9	156 – 174
H-P-O	115.3	113.9	–
O-Tl-O	88.16	83.58	80.61

Table 5. Optimised distances [pm] for $[Au(C_6H_5)_2]^-$ at the MP2 level.

Parameter	Au[19-VE] QR	Au[19-VE] NR	Experimental
Au−C	206.96	223.76	205.8
C−C1	139.42	141.33	137.5
C−C2	136 – 137	138 – 139	135 – 138

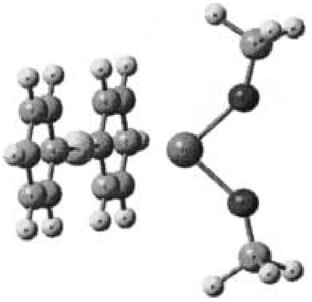

Figure 5. Theoretical model system $[Tl(OPH_3)_2][Au(C_6H_5)_2]$ in C_{2v} symmetry for ab initio calculations.

Table 6. Optimised Tl−Au distance R_e [pm], interaction energy $V(R_e)$ [kJ mol^{-1}] and F [N/m] for $[Au(C_6H_5)_2][Tl(OPH_3)_2]$ and $[Au(C_6F_5)\text{-}[Tl(OPPh_3)_2]$ at the MP2 and HF levels.

Model system	Method	R_e	$V(R_e)$	F
$[Au(C_6H_5)_2][Tl(OPH_3)_2]$	MP2-QR	302.8	– 275.70	34.2
	HF-QR	336.2	– 227.38	19.5
	MP2-NR	313.1	– 216.98	30.1
	HF-NR	400.3	– 159.47	2.98
$[Au(C_6F_5)[Tl(OPPh_3)_2]$	exptl	303 – 308		

We described the experimental structures by an idealized $[Tl(OPH_3)_2][Au(C_6H_5)_2]$ model (Figure 5) with C_{2v} symmetry. Table 6 summarises the Au−Tl interaction energies and equilibrium distances. The calculated distances fall in the same range as the experimental ones. With quasi-relativistic pseudopotentials, the Au−Tl distance at the HF level is larger than that obtained at MP2 level, the latter being very close to the experimental values. The energies at the HF and MP2 levels are in the range of electrostatic interactions. However, the energy difference between HF and MP2 is 57 kJ mol^{-1}. This is within the range of magnitude of dispersion-type van der Waals interactions with charge transfer.

We included nonrelativistic results for comparison with the quasirelativistic data to enable quantification of the relativistic effect in the Au−Tl metallophilic attraction. The interaction energy decreases by 21 % on going from relativistic to nonrelativistic pseudopotentials at the MP2 level of theory. The result at the HF-NR level is poor, with a much too long Au−Tl distance. This reflects the importance of electronic correlation and the relativistic effects in heavy atoms.

The MP2-QR calculation reproduces the structural trends found in the experimental data. On the other hand, the interaction energy at the MP2-QR level consists of 80 % of ionic interaction and 20 % of van der Waals interactions, assuming that the electrostatic interaction is responsible for the attractive behaviour at the HF level and that the additional stabilization obtained at the MP2 level is due to the introduction of dispersion-type correlation effects and charge-transfer contributions.

Optical properties and time-dependent (TD)-DFT calculations: Similar to the infinite gold–thallium chain $[Tl(OPPh_3)_2][Au(C_6F_5)_2]$ (**3**), whose structure and luminescence were described earlier, **1** and **2** both luminesce at room temperature (293 K) and at 77 K in the solid state (Figure 6 and Figure 7). The complexes have similar spectra with a complicated excitation profiles and maxima at 400 nm for **1** and 392 nm for **2** at room temperature, which lead to broad emissions at 497 and 501 nm, respectively.

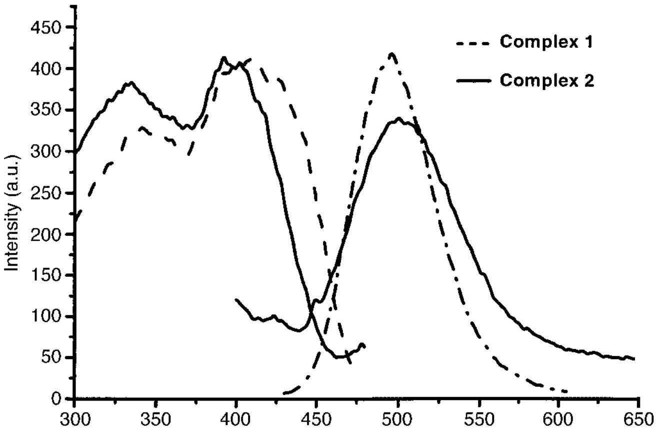

Figure 6. Luminescence spectra of complexes **1** and **2** at room temperature in the solid state.

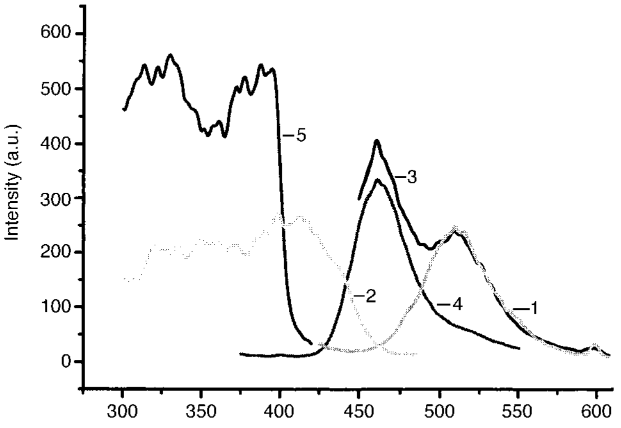

Figure 7. Luminescence spectra of **1** at 77 K in the solid state showing site-selective excitation.

The luminescence in these complexes is temperature-dependent, and also exhibits an interesting site-selective excitation at low temperatures, which is not observed at room temperature. Thus, we observe low-energy bands centred at 510 nm (line 1; excitation at 412 nm (line 2)) for **1** and at 526 nm (excitation at 408 nm) for **2**, and higher energy bands at 461 nm (line 4; excitation at 329 nm (line 5)) for **1** and at 465 nm (excitation at 334 nm) for **2** (see Figure 7).

The observation that the excitation and emission wavelengths are similar for the pairs of bands in both complexes seems to suggest the presence of similar fluorophores. Therefore, the excited states do not seem to be significantly influenced by the presence of different coordinating solvent molecules in the two complexes (THF in **1** and acetone in **2**); otherwise, a larger energy difference would be expected. In addition, since neither the gold(I) nor thallium(I) precursor complexes nor the ligands are luminescent at similar energies, and, furthermore, solutions of the complexes in acetone are colourless and do not show luminescence, while evaporation of the solvent regenerates the colour and the optical properties, we suggest that the extended-chain metal–metal interactions are responsible for the luminescence. Thus, the emissions are likely to result from electronic states that are strongly influenced by the interactions between the alternating gold and thallium centres. Hence, and with reference to previous theoretical work by Fackler et al.[11] and by us[8] on related gold–thallium chains, the orbitals which are responsible for light emission are considered to be mostly metal-based, with a greater influence of the thallium $6p_z$ orbital, and whose energy is largely influenced by the metal–metal separation, even though no formal metal–metal bond is present in the ground or excited states. However, in the above-mentioned cases, each alternating type of metal atom has a invariant coordination environment, which makes the analysis at each point of the infinite chain equivalent. By contrast, the presence of different environments around the thallium centres in the title complexes adds another factor that must be considered in addition to the metal–metal distance.

Thus, it seems likely that the emissions come from two different electronic states that can be related to the two coordination modes of the thallium centres, each of which in turn has different interactions with the gold atoms. In this regard, and as can be deduced from the theoretical study (see below), in these electronic states the geometry around the thallium centres is essential, rather than the gold–thallium interactions, which are responsible for the shifts in the emission band for each geometry. This assumption is in good agreement with experimental results on other linear gold–thallium chains[8] with distorted trigonal-bipyramidal environments and different gold–thallium interactions, because these do not show such site-selective excitation and the emission energies are close to the energy attributed to the thallium centres in the title complexes, which also have this environment (see below).

Therefore, in view of the results obtained by photophysical measurements and X-ray structural analysis, we performed single-point DFT calculations on simplified model systems of compounds **1** and **3**. Owing to the presence of different Au–Tl distances and Tl^I geometries in **1** we built four different dinuclear models **1a**–**1d** (Figure 8) to represent the four observed coordination environments (two distorted tetrahedral and two pseudo-trigonal-bipyramidal) and to study the influence of the intermetallic distances and the geometries around the Tl^I centres on the photophysical properties. Since

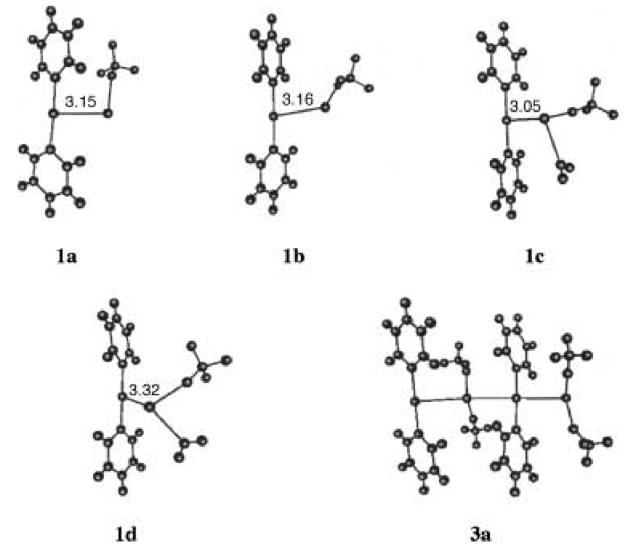

1a **1b** **1c** **1d** **3a**

Figure 8. Theoretical model systems **1a**–**1d** and **3a** for DFT and TD-DFT electronic-structure calculations.

3 consists of alternating Au- and Tl-centred counterions linked by Au–Tl interactions, we propose the tetranuclear model system **3a** to study the influence of the polymeric chain on the photophysical properties.

For **1** we studied the MOs and performed a population analysis from which we can deduce the contribution of each part of the molecule (metal atoms and ligands) to each occupied orbital for the four simplified models **1a**–**1d**. The results are given in Tables 7, 8, 9 and 10, which show that the occupied orbitals involved in the theoretical transitions (see TD-DFT calculations below) are mainly located on the $[AuR_2]^-$ units or at the gold centres, with no significant contribution from either the Tl^I centres or the O-donor ligands. On the other hand, the lowest unoccupied orbitals cannot be subjected to population analysis, but we can perform a visual analysis of their shape. Figure 9 shows the lowest unoccupied orbitals (involved in the theoretical transitions; see below) for models **1a** (distorted tetrahedral) and **1c** (pseudo-trigonal-bipyramidal) as representative examples of the different geometries around thallium centres, and it can be clearly seen that these orbitals are mainly thallium-based, with small contributions from gold centres in some cases. Thus, from this analysis it can be deduced that the highest occupied orbitals are mainly localised in the $[AuR_2]^-$ units or at the gold atoms, while the locations of the lowest

Table 7. Population analysis for $[Tl(OPH_3)][Au(C_6H_5)_2]$ (distorted-tetrahedral) model system **1a**. Percentage contribution from each type of atom to occupied orbitals.

MO	Au	Tl	C_6H_5	OPH_3
HOMO-1 (64a)	13.1	0.9	84.0	1.9
HOMO-5 (60a)	69.6	10.2	19.1	0.4
HOMO-7 (58a)	98.2	0.9	0.7	–
HOMO-8 (57a)	91.2	6.9	1.0	0.7

Table 8. Population analysis for $[Tl(OPH_3)][Au(C_6H_5)_2]$ (distorted-tetrahedral) model system **1b**. Percentage contribution from each type of atom to occupied orbitals.

MO	Au	Tl	C_6H_5	OPH_3
HOMO-1 (64a)	17.7	0.7	81.5	–
HOMO-3 (62a)	48.4	2.5	48.8	–
HOMO-4 (61a)	36.8	8.1	54.4	3.5
HOMO-5 (60a)	3.7	1.0	95.1	–
HOMO-7 (58a)	94.5	4.3	0.55	0.5
HOMO-8 (57a)	95.0	2.8	2.0	0.1

Table 9. Population analysis for $[Tl(OPH_3)(H_2O)][Au(C_6H_5)_2]$ (pseudo-trigonal-bipyramidal) model system **1c**. Percentage contribution from each type of atom to occupied orbitals.

MO	Au	Tl	C_6H_5	OPH_3, H_2O
HOMO (70a)	4.9	0.6	89.9	4.5
HOMO-1 (69a)	19.1	0.3	80.6	–
HOMO-2 (68a)	70.8	12.6	15.3	1.2
HOMO-3 (67a)	3.9	0.7	95.3	–
HOMO-4 (66a)	3.0	1.1	95.9	–
HOMO-5 (65a)	6.6	0.6	92.5	0.2
HOMO-6 (64a)	79.2	0.2	20.4	–
HOMO-7 (63a)	88.7	8.6	1.5	1.2
HOMO-8 (62a)	97.9	0.8	1.2	–

Table 10. Population analysis for $[Tl(OPH_3)(H_2O)][Au(C_6H_5)_2]$ (pseudo-trigonal-bipyramidal) model system **1d**. Percentage contribution from each type of atom to occupied orbitals.

MO	Au	Tl	C_6H_5	OPH_3, H_2O
HOMO (70a)	6.7	0.2	88.9	4.1
HOMO-1 (69a)	21.1	2.5	78.6	–
HOMO-2 (68a)	79.3	2.5	13.7	–
HOMO-4 (66a)	7.8	1.9	90.3	–
HOMO-5 (65a)	2.5	0.4	97.0	–

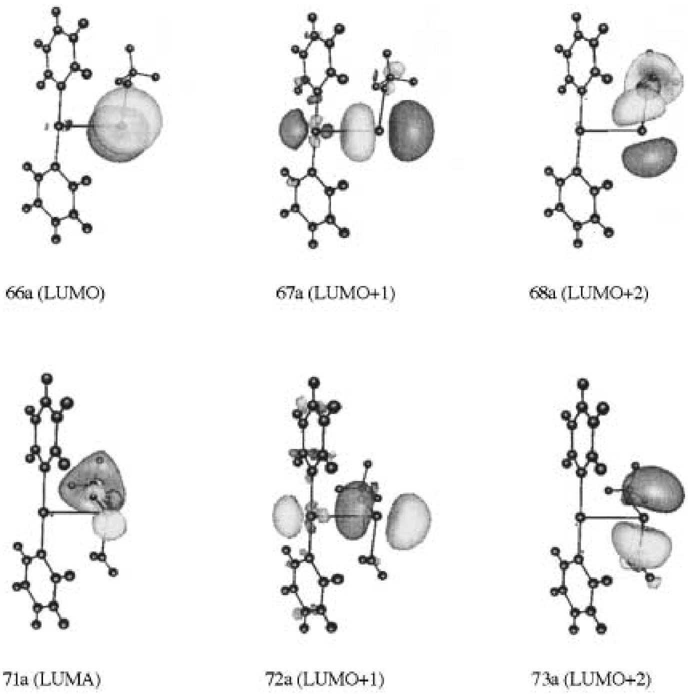

Figure 9. Lower energy virtual molecular orbitals for theoretical models **1a** (distorted tetrahedral) and **1c** (pseudo-trigonal-bipyramidal).

unoccupied orbitals shows that the potential fluorophores are the thallium centres, since they are the main contributors to the orbitals from which the emission is produced, although the contribution of the gold centres cannot be neglected.

The same type of analysis was carried out for model system **3a** (Figure 8). Both the molecular orbitals and the population analysis show the same trend as the dinuclear models for **1**. Thus, the occupied molecular orbitals are mainly $[AuR_2]^-$-based (Table 11) and the most important unoccupied orbital is 159a (LUMO + 2), a metal-based orbital (Figure 10) mainly localised on Tl^I. Therefore, the electronic structure of **3** is similar that of **1**: excitations come from $[AuR_2]^-$-based orbitals and enter a Tl^I-based orbital that acts as fluorophore for the emission of light.

The above conclusions were confirmed by TD-DFT calculations. Thus, the first few singlet excitation energies of **1a**–**1d** and **3a** were calculated at the TD–DFT level (see Methods of Calculation). Since we currently cannot estimate the contribution of spin–orbit effects to the triplet transitions, only singlet–singlet transitions were considered in these quasirelativistic calculations.

Table 11. Population analysis for $[Tl(OPH_3)_2][Au(C_6H_5)_2][Tl(OPH_3)_2]$-$[Au(C_6H_5)_2]$ model system **3a**. Percentage contribution from each type of atom to occupied orbitals.

MO	Au	Tl	C_6H_5	OPH_3
HOMO (156a)	4.7	0.2	95.1	–
HOMO-1 (155a)	63.9	22.2	11.7	2.1
HOMO-2 (154a)	28.2	0.2	71.5	–
HOMO-5 (151a)	7.7	1.1	91.1	–
HOMO-6 (150a)	20.6	0.4	78.6	0.3
HOMO-7 (149a)	40.4	3.5	55.4	0.7
HOMO-8 (148a)	45.3	0.1	53.4	1.1

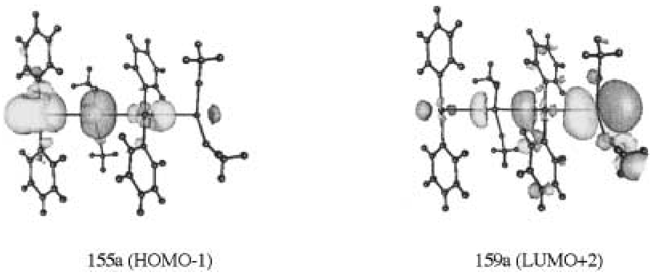
155a (HOMO-1) 159a (LUMO+2)

Figure 10. HOMO-1 (155a) and LUMO + 2 (159a) molecular orbitals for model **3a**.

As mentioned above, **1** and **2** show site-selective excitation at low temperature, with two independent pairs of excitation and emission bands at different energies. Hence, TD-DFT analysis was carried out for **1a** and **1b**, which have Tl^I centres in a pseudotetrahedral environment and two similar groups of excitations in the ranges 423–442 nm and 289–342 nm. The analysis of the theoretical transitions (Table 12 and Figure 11) shows for both ranges that the excitations originate from $[AuR_2]^-$- or Au^I-based orbitals and enter antibonding pseudotetrahedral Tl^I-based orbitals, that is, the antibonding Tl-

Table 12. TD-DFT RPA singlet-excitation calculations for simplified model systems **1a**–**1d** and **3a**.

Model **1a**	Model **1b**	Model **1c**	Model **1d**	Model **3a**
437.7 (0.034)[a]	442.0 (0.010)	374.3 (0.050)	404.0 (0.018)	445.3 (0.013)
64a → 67a (67)[b]	64a → 67a (83)	69a → 72a (54)	69a → 72a (62)	154a → 159a (100)
64a → 68a (20)	64a → 68a (8)	70a → 73a (32)	70a → 73a (35)	
423.4 (0.034)	428.6 (0.033)	371.8 (0.047)	398.5 (0.034)	425.8 (0.428)
64a → 68a (64)	64a → 68a (57)	70a → 73a (55)	70a → 73a (59)	155a → 159a (100)
64a → 67a (24)	62a → 66a (27)	69a → 72a (31)	69a → 72a (26)	
339.4 (0.014)	424.7 (0.019)	316.5 (0.011)	390.3 (0.010)	371.6 (0.010)
60a → 68a (78)	62a → 66a (69)	65a → 72a (37)	69a → 73a (100)	151a → 159a (100)
60a → 67a (13)	64a → 68a (26)	67a → 72a (31)		
326.8 (0.058)	342.5 (0.020)	312.5 (0.022)	327.1 (0.013)	353.6 (0.051)
58a → 66a (45)	64a → 69a (73)	68a → 73a (68)	66a → 72a (46)	150a → 159a (57)
60a → 67a (32)	60a → 68a (17)	65a → 72a (14)	68a → 73a (17)	149a → 159a (31)
310.6 (0.075)	339.4 (0.024)	306.4 (0.018)	319.3 (0.023)	352.1 (0.077)
58a → 66a (48)	60a → 68a (58)	66a → 73a (57)	66a → 73a (67)	149a → 159a (56)
60a → 67a (27)	64a → 69a (18)	67a → 73a (26)	66a → 72a (11)	150a → 159a (30)
	327.0 (0.093)	301.9 (0.077)	316.8 (0.072)	
	61a → 68a (43)	68a → 72a (23)	66a → 72a (23)	
	57a → 66a (23)	64a → 71a (17)	68a → 72a (21)	
	321.5 (0.011)	301.4 (0.017)	309.0 (0.027)	
	58a → 66a (95)	64a → 71a (80)	65a → 73a (84)	
	312.4 (0.042)	290.9 (0.018)	280.9 (0.056)	
	57a → 66a (67)	68a → 74a (38)	69a → 75a (58)	
	61a → 68a (11)	62a → 71a (30)	66a → 74a (14)	
	289.7 (0.010)			
	64a → 70a (54)			
	65a → 71a (35)			
	289.1 (0.011)			
	65a → 71a (60)			
	64a → 70a (29)			

[a] Energy of theoretical transitions in nanometres and oscillator strengths (in parentheses) that shows the mixed representation of both velocity and length. [b] Contributions to each transition. The value in parentheses is $|\text{coeff.}|^2 \times 100$.

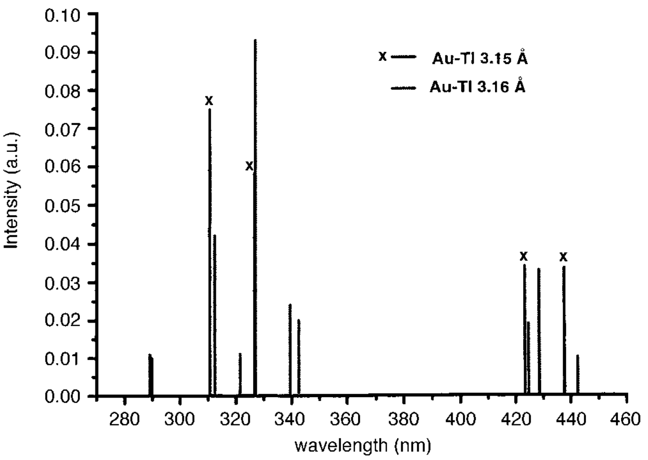

Figure 11. Theoretical excitation spectra for models **1a** and **1b** (distorted tetrahedral).

based molecular orbitals are responsible for the emission of light.

The TD-DFT analysis of **1c** and **1d**, which have Tl^I centres in a distorted trigonal-bipyramidal environment again gave two groups of excitations for each model (Figure 12). The low-energy range is 372 – 404 nm, and the high-energy range 281 – 327 nm. As in the pseudotetrahedral models, the the starting orbitals of the excitations are mainly centred on the $[AuR_2]^-$ units or at the Au^I centres, while the target orbitals are mainly antibonding Tl^I-based molecular orbitals (Table 12).

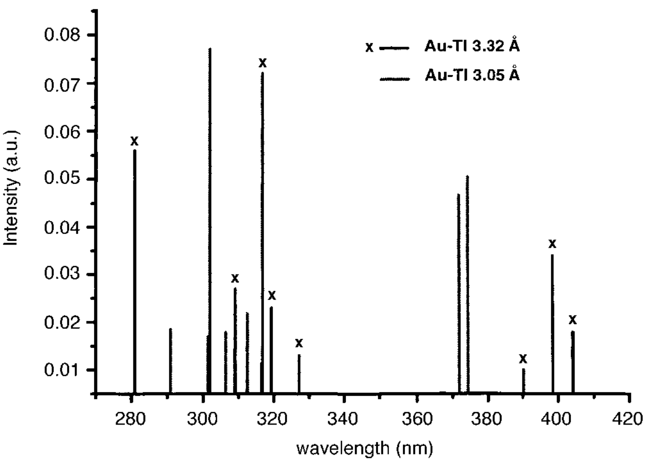

Figure 12. Theoretical excitation spectra for models **1c** and **1d** (pseudo-trigonal-bipyramidal).

Therefore, the theoretical excitations are in very good agreement with the two site-selective experimental excitation spectra of **1** (Figure 13). Careful inspection of the theoretical excitation spectra indicates that the lower energy excitations (420 – 450 nm) can be assigned to the $Au^I – Tl^I$ pseudotetrahedral interactions, while those at higher energy (around 280 nm) can be assigned to the $Au^I – Tl^I$ distorted trigonal-bipyramidal interactions. In fact, experimental excitation of **1** and **2** at low energy (412 and 408 nm, respectively) gives rise to single low-energy emissions (510 and 526 nm, respectively) that could be produced by emission of light from antibonding, pseudotetrahedral Tl(I) molecular orbitals. Excitation of **1** and **2** at high energy (329 and 334 nm, respectively) leads to single high-energy emissions (461 and 465 nm, respectively), perhaps from antibonding, distorted trigonal-bipyramidal Tl^I molecular orbitals. Finally, excitation in the range 340 – 405 nm gives rise to both emissions, in accordance with the theoretially determined availability of both types of Tl-based molecular orbitals as target orbitals in this energy range.

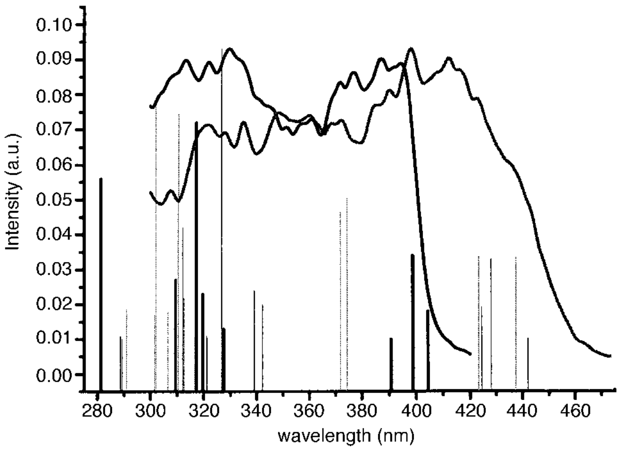

Figure 13. Comparison between theoretical (models **1a** – **1d**) and experimental excitation spectra for complex **1**.

We also carried out a TD-DFT calculation on **3a**, a simplified model system of **3**. We used this tetranuclear model, in which the Tl^I geometry is always distorted trigonal-bipyramidal, to analyze the influence of the polymeric Au – Tl chain on the photophysical behaviour. Table 12 lists the most important theoretical excitations for model **3a**. As shown in Figure 14, the theoretical spectrum clearly matches the experimental one, and theoretical excitation B at 425.8 nm is the most important. The analysis of this excitation shows that both the starting and the target orbitals are metal-based, whereby virtual orbital 159a, mainly localised on Tl^I, is the orbital from which the emission is produced in all cases,

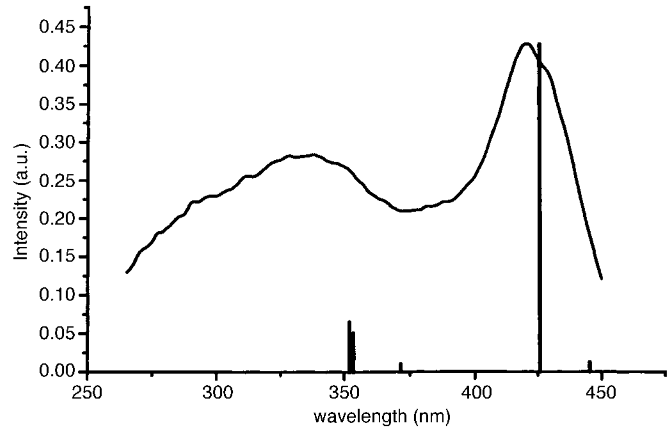

Figure 14. Comparison of theoretical and experimental excitation spectra for complex **3**.

although the contribution from gold atoms is also important for this orbital (Figure 10).

In short, the TD-DFT calculations confirm the qualitative explanation for the photophysical behavior of the Au–Tl complexes **1**–**3**. First, they explain the site-selective excitation of **1** and **2** due to the presence of different environments of Tl^I centers. In addition, we observed increasing metal-based character of the orbitals responsible for luminescence when we increased the nuclearity of the model system (i.e., **3a**), which matches the experimental spectra.

The basic conclusion is that the excitation has $AuR_2 \rightarrow Tl^I$ charge-transfer character, whereby the thallium centres act as fluorophores which are influenced by the presence of different environments of the Tl^I centres. This suggests that Tl–ligand interactions have a greater influence on the photoluminescence than Tl^I–Au^I interactions. Similar conclusions were recently drawn by Che et al. for d^{10}–d^{10} metal complexes.[22–24]

Experimental Section

Instrumentation: Infrared spectra were recorded in the range 4000–200 cm^{-1} on a Perkin-Elmer FT-IR Spectrum 1000 spectrophotometer with Nujol mulls between polyethylene sheets. C, H, N analyses were carried out with a C.E. Instrument EA-1110 CHNS-O microanalyzer. Mass spectra were recorded on a HP-5989B Mass Spectrometer API-Electrospray with interface 59987A. ^1H, ^{19}F and $^{31}P\{^1H\}$ NMR spectra were recorded on a Bruker ARX 300 in $(CD_3)_2CO$ or $CDCl_3$. Chemical shifts are quoted relative to $SiMe_4$ (^1H, external), $CFCl_3$ (^{19}F, external) and 85% H_3PO_4 (^{31}P, external). Excitation and emission spectra were recorded on a Perkin-Elmer LS-50B luminescence spectrometer. Acetone for photophysics was distilled over potassium permanganate and degassed before use. $NBu_4[AuR_2]$ ($R = C_6F_5$, C_6Cl_5) starting materials were prepared according to ref. [25].

Preparation of $[Tl(OPPh_3)(THF)][Au(C_6Cl_5)_2][Tl(OPPh_3)][Au(C_6Cl_5)_2]$ (1) and $[Tl(OPPh_3)(acetone)][Au(C_6Cl_5)_2][Tl(OPPh_3)][Au(C_6Cl_5)_2]$ (2): $OPPh_3$ (0.07 g, 0.26 mmol) was added to a solution of $TlPF_6$ (0.09 g, 0.26 mmol) and $NBu_4[Au(C_6Cl_5)_2]$ (0.24 g, 0.26 mmol) in THF (**1**; 35 mL) or acetone (**2**; 35 mL). The solutions were stirred for 30 min followed by evaporation of the solvents under vacuum. The resulting solids were washed with dichloromethane (20 mL) and collected by filtration to give **1** and **2** as green solids. Yield: 72% (**1**) and 65% (**2**). Crystals suitable for X-ray diffraction studies on **1** and **2** were obtained by slow diffusion of *n*-hexane into a concentrated solution of the complex in THF (**1**) or acetone (**2**). Elemental analysis (%) calcd for **1** ($C_{64}H_{38}Au_2Tl_2P_2Cl_{20}O_3$): C 31.65, H 1.6; found: C 31.8, H 1.7; elemental analysis (%) calcd for **2** ($C_{63}H_{36}Au_2Tl_2P_2Cl_{20}O_3$): C 31.35, H 1.50; found: C 31.0, H 1.45; $^{31}P\{^1H\}$ NMR (298 K, $(CD_3)_2CO$)), $\delta = 26.5$ (s) (**1**); 26.7 ppm (s) (**2**); ^1H NMR (298 K, $(CD_3)_2CO$)): $\delta = 7.56$–7.73 (m, 30H, Ph) (**1**); 7.54–7.70 (m, 30H, Ph) (**2**); 3.43, (m, 4H, THF), 1.86 (m, 4H, THF) (**1**); 2.09 ppm (s, 6H, acetone) (**2**); MS for **1** and **2**: *m/z* (%): 695 (100) $[Au(C_6Cl_5)_2]^-$ (ES–), 204 (100), Tl^+ (ES+).

Crystallography: The crystals were mounted in inert oil on glass fibres and transferred to the cold gas stream of a Nonius Kappa CCD diffractometer equipped with an Oxford Instruments low-temperature attachment. Data were collected with monochromatized $Mo_{K\alpha}$ radiation ($\lambda = 0.71073$ Å) by ω and ϕ type scans. Absorption corrections: numerical (based on multiple scans). The structures were solved by direct methods and refined on F^2 by using the program SHELXL-97.[26] All non-hydrogen atoms were refined anisotropically. Hydrogen atoms were included with a riding model. Further details of the data collection and refinement are given in Table 1. CCDC-187673 and CCDC-187674 contain the supplementary crystallographic data for this paper. These data can be obtained free of charge via www.ccdc.cam.ac.uk/conts/retrieving.html (or from the Cambridge Crystallographic Data Centre, 12 Union Road, Cambridge CB21EZ, UK; fax: (+44) 1223-336-033; or deposit@ccdc.cam.ac.uk).

Methods of calculation: *HF and MP2 calculations*: The Gaussian 98 package[27] was used. The basis sets and pseudopotentials (PP) used in the production run are given in Table 4. The 19-valence electron (VE) quasirelativistic (QR) and nonrelativistic (NR) PPs of Schwerdtfeger et al.[28] were employed for gold. For the thallium atom 3-VE QR and NR PPs were used.[29] We employed one f-type polarization function for Au and Tl centres. The f orbital is necessary for the weak intermolecular interactions, as was demonstrated previously for various metals.[1, 4, 30] The diffuse f orbital exponent for the Tl atom was obtained by maximizing the electric dipole polarizability of the Tl^I cation ($\alpha_f = 0.34$). The atoms C, P and O were also treated by Stuttgart pseudopotentials,[31] including only the valence electrons for each atom. For these atoms, double-zeta basis sets were used, augmented by d-type polarization functions. For the H atom, a double-zeta and one p-type polarization function were used (see Table 13).[32]

Table 13. Basis sets and pseudopotentials (PPs) used in the present work.

Atom	PP	Basis	Remarks
H	–	(4s1p)/[2s1p]	$\alpha_p = 0.80$
C	Bergner 4-VE	(4s4p1d)/[2s2p1d]	$\alpha_d = 0.80$
P	Bergner 5-VE	(4s4p1d)/[2s2p1d]	$\alpha_d = 0.34$
O	Bergner 6-VE	(4s4p1d)/[2s2p1d]	$\alpha_d = 1.154$
Au	Schwerdtfeger QR 19-VE	(8s6p5d1f)/[7s3p4d1f]	$\alpha_f = 0.20$
Au	Schwerdtfeger NR 19-VE	(8s6p5d1f)/[8s3p4d1f]	$\alpha_f = 0.20$
Tl	QR 3-VE	(4s4p1d1f)/[2s2p1d1f]	$\alpha_f = 0.34$
Tl	NR 3-VE	(4s4p1d1f)/[2s2p1d1f]	$\alpha_f = 0.34$

First, we studied the experimental compounds using the model $[Tl(OPH_3)_2][Au(C_6H_5)_2]$. We replaced the groups $OPPh_3$ by OPH_3 and C_6F_5 by C_6H_5. We optimised the structures $[Tl(OPH_3)_2]^+$ and $[Au(C_6H_5)_2]^-$ separately at the second-order Møller–Plesset (MP2) level of perturbation theory (see Figure 5).[33] We studied the intermolecular interactions by comparing the Au–Tl distances obtained at the Hartree-Fock (HF) and MP2 levels of theory with both QR and NR pseudopotentials. The interaction energies were calculated by using the method of counterpoise correction. Therefore, the basis sets superposition error (BSSE) is corrected in these analyses.

TD-DFT calculations: The molecular structures used in the theoretical studies on $[Tl(OPH_3)_2][Au(C_6H_5)_2][Tl(OPH_3)(H_2O)][Au(C_6H_5)_2]$ (**1a**) and $[Tl(OPH_3)_2][Au(C_6H_5)_2][Tl(OPH_3)_2][Au(C_6H_5)_2]$ (**3a**) were taken from the X-ray diffraction data for $[Au(C_6Cl_5)_2]_2[Tl(OPPh_3)][Tl(OPPh_3)(THF)]$ (**1**) and $[Tl(OPPh_3)_2][Au(C_6F_5)_2]$ (**3**), respectively. Keeping all distances, angles and dihedral angles frozen, single-point DFT calculations were performed on the models. In both the single-point ground-state calculations and the subsequent calculations of the electronic excitation spectra, the default Beck–Perdew (BP) functional[34–36] as implemented in TURBOMOLE[37] was used. The excitation energies were obtained at the density functional level by using the time-dependent perturbation theory approach (TD-DFT),[38–42] which is a DFT generalization of the Hartree–Fock linear response (HF-LR) or random-phase approximation (RPA) method.[43]
In all calculations, the Karlsruhe split-valence quality basis sets[44] augmented with polarization functions[45] were used (SVP). The Stuttgart effective core potentials in TURBOMOLE were used for Au and Tl.[46] Calculations were performed without any assumption of symmetry for **1a**–**1d** and **3a**.

Acknowledgements

We thank the MCYT/FEDER (BQU2001-2409), Projects CSIC (España)-CONICYT (Chile) and Fondecyt N° 1020141 (Chile).

---

[1] P. Pyykkö, *Chem. Rev.* **1997**, *97*, 597.
[2] a) H. Schmidbaur, *Gold Bull.* **1990**, *23*, 11; b) H. Schmidbaur, *Chem. Soc. Rev.* **1995**, *24*, 391. c) H. Schmidbaur, *Gold Bull.* **2000**, *33*, 1.

[3] a) L. H. Gade, *Angew. Chem.* **1997**, *109*, 1219; *Angew. Chem. Int. Ed. Engl.* **1997**, *36*, 1171; b) J. M. Forward, J. P. Fackler, Jr., Z. Assefa in *Optoelectronic Properties of Inorganic Compounds* (Eds.: D. M. Roundhill, J. P. Fackler, Jr.), Plenum, New York, **1999**, p. 195; c) V. W. W. Yam, K. K. W. Lo, *Chem. Soc. Rev.* **1999**, *28*, 323.

[4] O. Crespo, A. Laguna, E. J. Fernández, J. M. López-de-Luzuriaga, P. G. Jones, M. Teichert, M. Monge, P. Pyykkö, N. Runeberg, M. Schütz, H.-J. Werner, *Inorg. Chem.* **2000**, *39*, 4786.

[5] a) P. Pyykkö, N. Runeberg, F. Mendizabal, *Chem. Eur. J.* **1997**, *3*, 1451; b) E. J. Fernández, J. M. López-de-Luzuriaga, M. Monge, M. A. Rodríguez, O. Crespo, M. C. Gimeno, A. Laguna, P. G. Jones, *Chem. Eur J.* **2000**, *6*, 636.

[6] E. J. Fernández, J. M. López-de-Luzuriaga, O. Crespo, A. Laguna, P. G. Jones, M. Monge, P. Pyykkö, N. Runeberg, *Eur. J. Inorg. Chem.* **2002**, 750.

[7] E. J. Fernández, M. C. Gimeno, A. Laguna, J. M. López-de-Luzuriaga, M. Monge, P. Pyykkö, D. Sundholm, *J. Am. Chem. Soc.* **2000**, *122*, 7287.

[8] O. Crespo, E. J. Fernández, P. G. Jones, A. Laguna, J. M. López-de-Luzuriaga, A. Mendía, M. Monge, M. E. Olmos, *Chem. Commun.* **1998**, 2233.

[9] E. J. Fernández, P. G. Jones, A. Laguna, J. M. López-de-Luzuriaga, M. Monge, M. E. Olmos, J. Pérez, *Inorg. Chem.* **2002**, *41*, 1056.

[10] E. J. Fernández, A. Laguna, J. M. López-de-Luzuriaga, *Gold Bull.* **2001**, *34*, 14.

[11] S. Wang, G. Garzon, C. King, J.-C. Wang, J. P. Fackler, Jr., *Inorg. Chem.* **1989**, *28*, 4623.

[12] A. Burini, R. Bravi, J. P. Fackler, Jr., R. Galassi, T. A. Grant, M. A. Omary, B. R. Pietroni, R. J. Staples, *Inorg. Chem.* **2000**, *39*, 3158.

[13] V. J. Catalano, B. L. Bennett, H. M. Kar, *J. Am. Chem. Soc.* **1999**, *121*, 10235.

[14] L. H. Gade, *Angew. Chem.* **2001**, *113*, 3685; *Angew. Chem. Int. Ed.* **2001**, *40*, 3573.

[15] N. G. Connelly, O. M. Hicks, G. R. Lewis, M. T. Moreno, A. G. Orpen, *J. Chem. Soc. Dalton Trans.* **1998**, 1913.

[16] J.-Y. Tung, J.-H. Chen, F.-L. Liao, S.-L. Wang, L.-P. Hwang, *Inorg. Chem.* **1998**, *37*, 6104.

[17] G. A. Abakumov, V. K. Cherkasov, V. I. Nevodchikov, V. A. Kuropatov, B. C. Noll, C. G. Pierpont, *Inorg. Chem.* **1998**, *37*, 6117.

[18] I. Ara, J. R. Berenguer, J. Forniés, J. Gómez, E. Lalinde, R. I. Merino, *Inorg. Chem.* **1997**, *36*, 6461.

[19] O. Renn, B. Lippert, I. Mutikainen, *Inorg. Chim. Acta* **1993**, *208*, 219.

[20] A. L. Balch, S. D. Rowley, *J. Am. Chem. Soc.* **1990**, *112*, 6139.

[21] A. L. Balch, F. Neve, M. M. Olmstead, *J. Am. Chem. Soc.* **1991**, *113*, 2995.

[22] W. F. Fu, K. C. Chan, V. M. Miskowsky, C. M. Che, *Angew. Chem.* **1999**, *111*, 2953; *Angew. Chem. Int. Ed.* **1999**, *38*, 2783.

[23] W. F. Fu, K. C. Chan, K. K. Cheung, C. M. Che, *Chem. Eur. J.* **2001**, *7*, 4656.

[24] H. X. Zhang, C. M. Che, *Chem. Eur. J.* **2001**, *7*, 4887.

[25] R. Usón, A. Laguna, *Coord. Chem. Rev.* **1986**, *70*, 1.

[26] G. M. Sheldrick, SHELXL-97, A program for crystal structure refinement, University of Göttingen, Göttingen, Germany, **1997**.

[27] Gaussian 98, M. J. Frisch, G. W. Trucks, H. B. Schlegel, P. M. W. Gill, B. G. Johnson, M. A. Robb, J. R. Cheeseman, K. T. Keith, G. A. Petersson, J. A. Montgomery, K. Raghavachari, M. A. Al-Laham, V. G. Zakrzewski, J. V. Ortiz, J. B. Foresman, J. Cioslowski, B. B. Stefanov, A. Nanayakkara, M. Challacombe, C. Y. Peng, P. Y. Ayala, W. Chen, M. W. Wong, J. L. Andres, E. S. Replogle, R. Gomperts, R. L. Martin, D. J. Fox, J. S. Binkley, D. J. Defrees, J. Baker, J. P. Stewart, M. Head-Gordon, C. Gonzalez, J. A. Pople, Gaussian, Inc., Pittsburgh, PA, **1998**.

[28] P. Schwerdtfeger, M. Dolg, W. H. E. Schwardz, G. A. Bowmaker, P. D. W. Boyd, *J. Chem. Phys.* **1989**, 91, 1762.

[29] W. Kuechle, M. Dolg, H. Stoll, H. Preuss, *Mol. Phys.* **1991**, 74, 1245.

[30] a) P. Pyykkö, F. Mendizabal, *Inog. Chem.* **1998**, *37*, 3018; b) N. Runenberg, M. Schütz, H.-J. Werner, *J. Chem. Phys.* **1999**, *110*, 7210.

[31] A. Bergner, M. Dolg, W. Küchle, H. Stoll, H. Preuss, *Mol. Phys.* **1993**, *80*, 1431.

[32] T. H. Dunning, P. J. Hay in *Modern Theoretical Chemistry*, *Vol. 3* (Ed.: H. F. Schaefer), Plenum Press, New York, **1997**, pp. 1–28.

[33] C. Møller, M. S. Plesset, *J. Chem. Phys.* **1934**, *46*, 618.

[34] S. H. Vosko, L. Wilk, M. Nusair, *Can. J. Phys.* **1980**, *58*, 1200.

[35] J. P. Perdew, *Phys. Rev. B* **1986**, *33*, 8822.

[36] A. D. Becke, *Phys. Rev. B* **1988**, *38*, 3098.

[37] R. Ahlrichs, M. Bär, M. Häser, H. Horn, C. Kölmel, *Chem. Phys. Lett.* **1989**, *162*, 165.

[38] R. Bauernschmitt, R. Ahlrichs, *Chem. Phys. Lett.* **1996**, *256*, 454.

[39] R. Bauernschmitt, R. Ahlrichs, *J. Chem. Phys.* **1996**, *104*, 9047.

[40] R. Bauernschmitt, M. Häser, O. Treutler, R. Ahlrichs, *Chem. Phys. Lett.* **1997**, *264*, 573, and refs. therein.

[41] E. K. U. Gross, W. Kohn, *Adv. Quantum Chem.* **1990**, *21*, 255.

[42] M. E. Casida in *Recent Advances in Density Functional Methods*, *Vol. 1* (Ed.: D. P. Chong), World Scientific, River Edge, NJ, **1995**.

[43] J. Olsen, P. Jørgensen in *Modern Electronic Structure Theory*, *Vol. 2* (Ed.: D. R. Yarkony), World Scientific, River Edge, NJ, **1995**.

[44] A. Schäfer, H. Horn, R. Ahlrichs, *J. Chem. Phys.* **1992**, *97*, 2571.

[45] T. H. Dunning, Jr., *J. Chem. Phys.* **1994**, *100*, 5829.

[46] D. Andrae, U. Haeussermann, M. Dolg, H. Stoll, H. Preuss, *Theor. Chim. Acta* **1990**, *77*, 123.

Received: June 24, 2002 [F4203]